CrossMark

Nanopowders of gallium nitride GaN surface functionalized with manganese

Michał Musiał[1], Jacek Gosk[2], Andrzej Twardowski[3], Jerzy F. Janik[1], and Mariusz Drygaś[1,*]

[1] *Faculty of Energy and Fuels, AGH University of Science and Technology, al. Mickiewicza 30, 30-059 Krakow, Poland*

[2] *Faculty of Physics, Warsaw University of Technology, ul. Koszykowa 75, 00-662 Warsaw, Poland*

[3] *Faculty of Physics, Institute of Experimental Physics, University of Warsaw, ul. Pasteura 2, 02-093 Warsaw, Poland*

ABSTRACT

Four GaN nanopowders of systematically varying surface properties, prepared via an anaerobic synthesis method from gallium imide (ammonia assisted decomposition in the range 600–975 °C), were subjected to functionalization with manganese centers. Each powder was slurried in a diluted hexane solution of manganese (II) bis{bis[trimethylsilyl]amide} $Mn\{N[Si(CH_3)_3]_2\}_2$ and stirred overnight at ambient conditions. This was followed by filtering out of the solid, rinsing it with hexane to remove excess of the manganese precursor, and evacuating volatiles. The raw solid with some adsorbed Mn precursor was then subjected to transamination/deamination chemistry at 200 °C, 18 h, under a flow of ammonia to afford Mn surface-functionalized GaN nanopowders. The powders were thoroughly characterized including investigation of their magnetic properties with a SQUID magnetometer. They were confirmed to have tightly bound manganese and significantly modified surface properties with relatively decreased BET specific surface areas and helium densities. Magnetic measurements were consistent with the formation of a paramagnetic surface (Ga,Mn)N-type of phase and some antiferromagnetic by-product, the latter formed from adventitious oxidation of excessive quantities of the manganese precursor.

Introduction

Throughout many years, now, there have been mind boggling concepts presented in functional materials design, synthesis, and applications which thrive on the specificity of nanoscopic material dimension and resulting novel properties and some recent reviews in the area are at hand [1–7]. They also include work on magnetic properties in the nanosized regime [6, 7] of which some aspects are of interest in the present study.

The advantageous physical and chemical properties of gallium nitride GaN, including the broad bandgap semiconducting characteristics, are the basis for its seminal applications as a blue light emitter in optoelectronics and as an indispensable component

Address correspondence to E-mail: madrygas@agh.edu.pl

🖄 Springer

in high-power and high-frequency electronic devices [8–20]. The relatively easily engineered bandgap, type of conductivity, and carrier concentration in monocrystalline and thin film forms of GaN are increasingly exploited in modern technologies. In this regard, the so-called diluted magnetic semiconductors DMS are of special interest in spintronics—the area that dwells on utilization of materials with both semiconducting and magnetic properties. The theoretical calculations suggest that GaN suitably doped with magnetic centers could become a DMS with a Curie temperature higher than room temperature and, therefore, suitable for many practical applications [21–23]. The magnetic dopants include such transition metals as Mn, Fe, Cr, Ni, and V, which should be substituted in metal sites of the GaN lattice [24–28].

In addition to monocrystals and thin films, GaN nanopowders are yet another material forms to be considered for such modifications aimed at specific applications. There have been reports on Mn incorporation in the nanopowders at up to 7–10 at.% levels [29, 30]. However, the most common shortcoming of these attempts was a formation/retention of detrimental ferromagnetic oxygen-bearing residues. The authors of this study managed the successful syntheses of Mn-doped bulk GaN nanopowders utilizing either the aerosol-assisted [31] or anaerobic decomposition of gallium imide [32–36] synthesis methods. In both cases, Mn concentrations of the order of 2–4 at.% incorporated in the hexagonal polytype of GaN were achieved. It has become apparent to us that there were definite limits in Mn incorporation because of balancing the thermodynamic stabilities of the pure and doped lattices with consequences of by-product formation due to dopant excessive quantities.
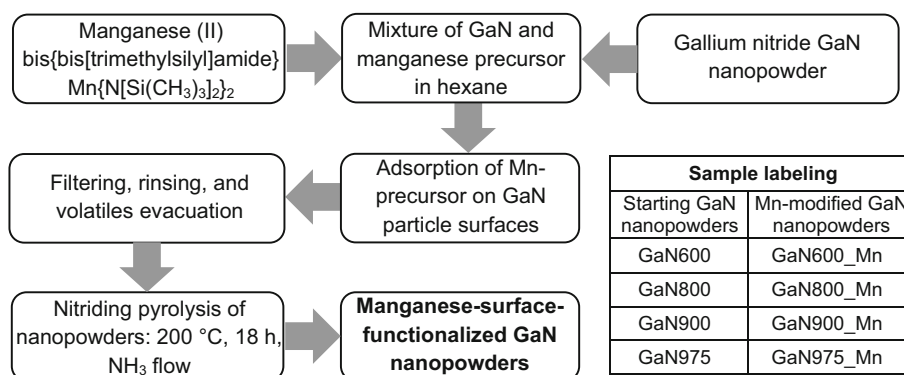
Facing limitations of this sort, an intriguing question arises as to a possibility for the utilization of high surface area of GaN nanopowders [37–40] for particle surface modifications with magnetic manganese centers to lead to a novel class of DMS—Mn surface-functionalized gallium nitride. The specific surface energetics coupled with the presence of reactive groups can in principle support Mn precursor chemisorption on particle surfaces. The most feasible post-reaction surface groups on GaN particles include Ga-NH$_2$ and Ga-N(H)-Ga. For instance, transamination reactions in the system involving such surface groups and an amide type of manganese precursor would result in definite coupling processes such as Ga-

NH$_2$ + (R$_2$N)-Mn → Ga-N(H)-Mn + ↑H(NR$_2$),   R = organic ligand, or according to Ga-NH$_2$ + H$_2$N-Mn → Ga-N(H)-Mn + ↑NH$_3$ in both cases yielding mixed metal–nitrogen bonds. Similarly, molecules of adsorbed NH$_3$ would react along the pathway Mn-(R$_2$N) + NH$_3$ → Mn-NH$_2$ + ↑H(NR$_2$) yielding the Mn-NH$_2$ species to react further with the gallium nitride surface groups. It is to be noted that one deals with both the surface of single nanocrystallites and the surface of agglomerates made of nanocrystallites of which relative proportion is predominantly the function of crystallite size in the low nanosized region [40]. The experimental manifestation of this aspect is a complex relationship between the average crystallite size and both the BET specific surface area and the helium density of a crystalline nanopowder. A specific interplay between the agglomeration affinity and surface and pore size characteristics will, therefore, determine the size of accessible surface for precursor modification in such systems. Such modified GaN nanopowders with targeted magnetic properties and type of conductivity, if achieved, could then be tried to be sintered into robust ceramics [35], which would offer prospects for potential DMS applications.

In order to eliminate/minimize oxygen impurity, an anaerobic synthesis and oxygen-free manganese (II) bis{bis[trimethylsilyl]amide} Mn{N[Si(CH$_3$)$_3$]$_2$}$_2$ were considered. Facing an unavailability of a preferred amide Mn[N(CH$_3$)$_2$]$_2$, this manganese silylamide precursor was successfully used by us for Mn incorporation in bulk GaN nanopowders [33, 34] including a study on subsequent no-additive sintering of such nanopowders [35]. The pure precursor undergoes efficient transamination/deamination reactions leading to η-Mn$_2$N$_3$ already upon ammonolytical pyrolysis at 150 °C [36]. It is worth to underline that there are known many polytypes of manganese nitride each stable in a definite temperature range [41, 42]. These phases are characteristic of diverse magnetic behavior from antiferromagnetic to ferrimagnetic depending on the structure and Mn/N stoichiometry [43–45].

Herein, chemisorption of Mn{N[Si(CH$_3$)$_3$]$_2$}$_2$ on a variety of GaN nanopowders and subsequent ammonolytical transamination/deamination chemistry was utilized to form thin layers of manganese nitrido species on gallium nitride particles. A pool of GaN nanopowders was first prepared via the anaerobic gallium imide decomposition method [46]. The application of different synthesis temperatures

Figure 1 Preparation of manganese surface-functionalized GaN nanopowders. Table in the *right corner* contains sample labels.

| | Manganese (II) bis{bis[trimethylsilyl]amide} Mn{N[Si(CH₃)₃]₂}₂ | → | Mixture of GaN and manganese precursor in hexane | ← | Gallium nitride GaN nanopowder |

Figure flow chart:

Manganese (II) bis{bis[trimethylsilyl]amide} $Mn\{N[Si(CH_3)_3]_2\}_2$ → Mixture of GaN and manganese precursor in hexane ← Gallium nitride GaN nanopowder

Filtering, rinsing, and volatiles evacuation ← Adsorption of Mn-precursor on GaN particle surfaces

Nitriding pyrolysis of nanopowders: 200 °C, 18 h, NH₃ flow → **Manganese-surface-functionalized GaN nanopowders**

Sample labeling	
Starting GaN nanopowders	Mn-modified GaN nanopowders
GaN600	GaN600_Mn
GaN800	GaN800_Mn
GaN900	GaN900_Mn
GaN975	GaN975_Mn

afforded a range of materials with varying average crystallite sizes and BET specific surface areas as well as with diverse helium densities. Upon saturation of hexane slurry containing a GaN powder and the soluble manganese precursor, a follow-up processing yielded the surface-functionalized product. All products were thoroughly characterized including a study of their magnetic properties.

Experimental

All reactions and manipulations were carried out under strict anaerobic conditions utilizing standard Schlenk technique and dry-box equipment. The synthesis of four starting GaN nanopowders was accomplished by using the known gallium imide decomposition route [46] under an ammonia flow of 0.05 L/min at 600, 800, 900, and 975 °C for 4 h. The materials were thoroughly characterized including studies of their structural, electronic, and morphological features. The Mn precursor, $Mn\{N[Si(CH_3)_3]_2\}_2$, was prepared via a modified metathesis reaction of $LiN[Si(CH_3)_3]_2$ and anhydrous manganese (II) chloride $MnCl_2$ in diethyl ether; the compound was demonstrated to be dimeric $\{Mn\{N[Si(CH_3)_3]_2\}_2\}_2$ in the solid state [47]. Upon final vacuum distillation, the precursor was obtained in the form of pink crystals. 10 mg of the precursor was dissolved in 20 mL of dry hexane affording a pinkish solution to which 1 g of a GaN nanopowder was added (nominal atomic ratio Ga/Mn equal ca. 450/1). The resulting slurry was stirred for 18 h at ambient conditions, and the solid was filtered and rinsed thrice on the frit with 20 mL of pure hexane each time to remove an excess/not adsorbed solute. Upon evacuation of volatiles, the solid product was heated in a flask under a flow of ammonia, 0.05 L/min, 200 °C, for 18 h to promote

transamination/deamination chemistry of the surface-attached Mn precursor. The procedure afforded four Mn surface-functionalized GaN nanopowders as shown in Fig. 1 that includes also the sample names.

The prepared starting and final materials were characterized by methods such as powder XRD diffractometry (PANalytical Empyrean, Cu Kα; $2\theta = 20$–$80°$; average crystallite sizes calculated from Scherrer equation), FT-IR (Nicolet 380, KBr pellets made in dry-box), UV–vis (Perkin-Elmer spectrophotometer Lambda 35 equipped with a 50 mm integrating sphere), photoelectron XPS spectroscopy (Vacuum Systems Workshop Ltd., Mg anode with photon energy of 1253.6 eV), and SEM/EDX examination (Hitachi Model S-4700). Study of surface properties included measurements of helium densities (Micromeritics AccuPyc) and BET specific surface areas, the latter determined from low-temperature nitrogen adsorption (Micromeritics Gemini 2380). Additionally, for the starting nanopowders, TGA/MS determinations were carried out (TA Instruments Q5000IR thermobalance with Pfeiffer ThermoStar mass spectrometer used for analysis of gas products; samples of 15–20 mg, argon flow, heating rate 10 °C/min, 50–1000 °C range). Magnetization of the Mn-functionalized nanopowders was measured as a function of magnetic field (up to 7 Tesla) and of temperature (2–400 K) using a SQUID magnetometer. For all samples, a diamagnetic contribution of the host GaN material and of the sample holder was taken into account.

Results and discussion

The representative examples of the XRD patterns are included in Fig. 2 for the 600 and 975 °C-processed nanopowders. The structure parameters derived from the XRD determinations for all materials are

Figure 2 XRD patterns for selected GaN nanopowders before and after Mn surface functionalization. *Top row* 600 °C-derived materials, *middle row* 975 °C-derived materials, *bottom row* reference *bar charts* for hexagonal GaN (*left*) and cubic GaN (*right*).
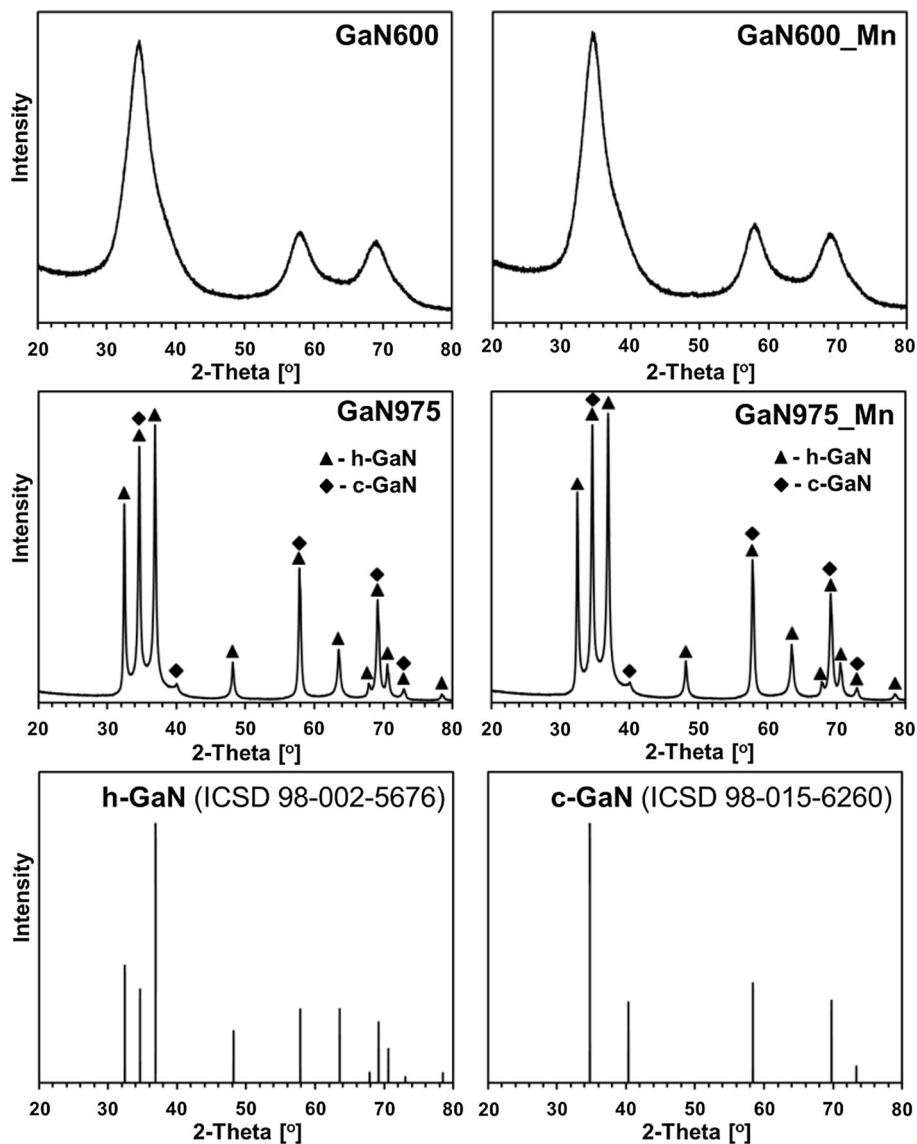

presented in Table 1. The two powders from the lowest synthesis temperature of 600 °C (top row, before and after Mn functionalization) show very similar patterns, if not identical, consisting of three very broad peaks (halos) suggesting extremely low crystallinity. They are best fitted assuming the cubic GaN polytype with average crystallite size of ca. 2 nm. This kind of pattern is typical for GaN on the verge of crystallinity and the actual phase inhomogeneous structure of such nanocrystallites is then suitably described as made of hexagonal and cubic closed-packed layers [46, 48]. Both powders from the 975 °C processing consist of the predominant hexagonal GaN (77–78 %, av. crystallite size of 75 nm) with the remaining minor cubic GaN (23 %,

av. crystallite size of 26 nm). The highest content of cubic GaN is found in the 800 °C-processed materials (86–88 %), whereas in the 900 °C-processed materials, both polytypes are in comparable quantities. It is evident that Mn functionalization of GaN particle surfaces has no detectable effect on standard structure parameters derived from XRD determinations. In summary of this aspect, the nanopowders are mixtures of two GaN polytypes. The hexagonal polytype shows the average crystallite size spanning 35–75 nm. The average crystallite size of the cubic polytype is significantly lower and ranges from 2 to 26 nm.

Thermal stability of the starting nanopowders was studied by TGA coupled with mass spectroscopic

Table 1 Structural properties of GaN nanopowders before and after Mn surface functionalization

| Samples	Phase content (%)		Lattice parameters (Å)		Average crystallite size (nm)	
	h-GaN	c-GaN	h-GaN	c-GaN	h-GaN	c-GaN
GaN600	–	100	–	4.53	–	2
GaN600_Mn	–	100	–	4.53	–	2
GaN800	14	86	$a = 3.19$ $c = 5.18$	$a = 4.50$	35	5
GaN800_Mn	12	88	$a = 3.19$ $c = 5.19$	$a = 4.51$	35	5
GaN900	54	46	$a = 3.19$ $c = 5.19$	$a = 4.50$	67	12
GaN900_Mn	50	50	$a = 3.19$ $c = 5.19$	$a = 4.50$	67	12
GaN975	77	23	$a = 3.19$ $c = 5.19$	$a = 4.50$	75	26
GaN975_Mn	78	22	$a = 3.19$ $c = 5.19$	$a = 4.50$	75	26
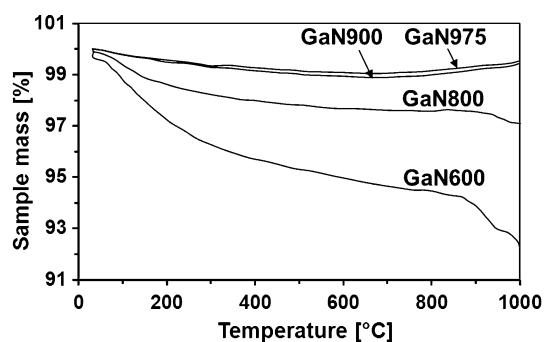
Figure 3 TGA traces of starting GaN nanopowders.

analysis of evolved gases. The curves of sample mass changes with temperature are shown in Fig. 3. The nanopowders from the highest synthesis temperatures of 900 and 975 °C are the most robust and stable among all samples—their curves pretty much overlap and indicate merely small decreases of mass of the order of a fraction of a percent taking place at relatively low temperatures. Above 750–800 °C, the curves start to bend upwards which is consistent with oxidation of GaN due to residual oxygen in argon gas. The 800 °C-processed nanopowder initially shows a faster and more extensive mass loss of up to ca. 2 wt%, whereas a steeper mass decrease above 900 °C indicates a beginning of nanopowder decomposition. A similar but even more pronounced changes of this type takes place for the nanopowder from the lowest synthesis temperature of 600 °C. Here, the initial low-temperature mass loss is of the order of 4–6 wt% and compound decomposition

starts at 800–850 °C. The observed trends are consistent with enhanced thermal stability of the high temperature-derived nanopowders, which can be linked to their structural integrity, larger average crystallite sizes/better crystallinity, and smaller specific surface areas compared with the low-temperature counterparts. The significant mass losses for the low temperature-derived nanopowders (600 and 800 °C) can be linked to increased quantities of adsorbed gases but, equally, to decomposition of abundant surface groups with volatiles formation. The mass spectroscopic analysis of evolved gases confirmed the presence of some adsorbed water and ammonia, the latter possibly originating also from deamination of surface amide groups according to Ga-NH$_2$ + H$_2$N-Ga → Ga-N(H)-Ga- + ↑NH$_3$. The gases were especially abundant for the reactive low temperature-derived nanopowders.

The FT-IR spectra for the 600 and 975 °C-processed nanopowders are shown in Fig. 4. All spectra contain a strong band at 560–570 cm^{-1} for Ga-N stretches in GaN. This is the only band in the 975 °C-materials, whereas, especially, in the 600 °C-materials, there are also other bands present. Those at ca. 970 and 2100 cm^{-1} can be traced to N≡C stretches in amorphous impurities resulting from thermal decomposition of residual dimethylamide groups in the gallium imide precursor [46]. The very broad band at ca. 3440 and small intensity band at 1630 cm^{-1} are typical for adsorbed water. The medium intensity peak at 3150–3200 cm^{-1} and the small intensity peak at 1500–1550 cm^{-1} are in the regions of N–H

Figure 4 FT-IR spectra for selected GaN nanopowders before and after Mn surface functionalization. *Top row* 600 °C-derived materials, *bottom row* 975 °C-derived materials. *Circles* show areas for various vibrations of residual N[Si(CH₃)₃]₂ groups; *vertical solid lines* indicate the position of Ga-N stretches in GaN.
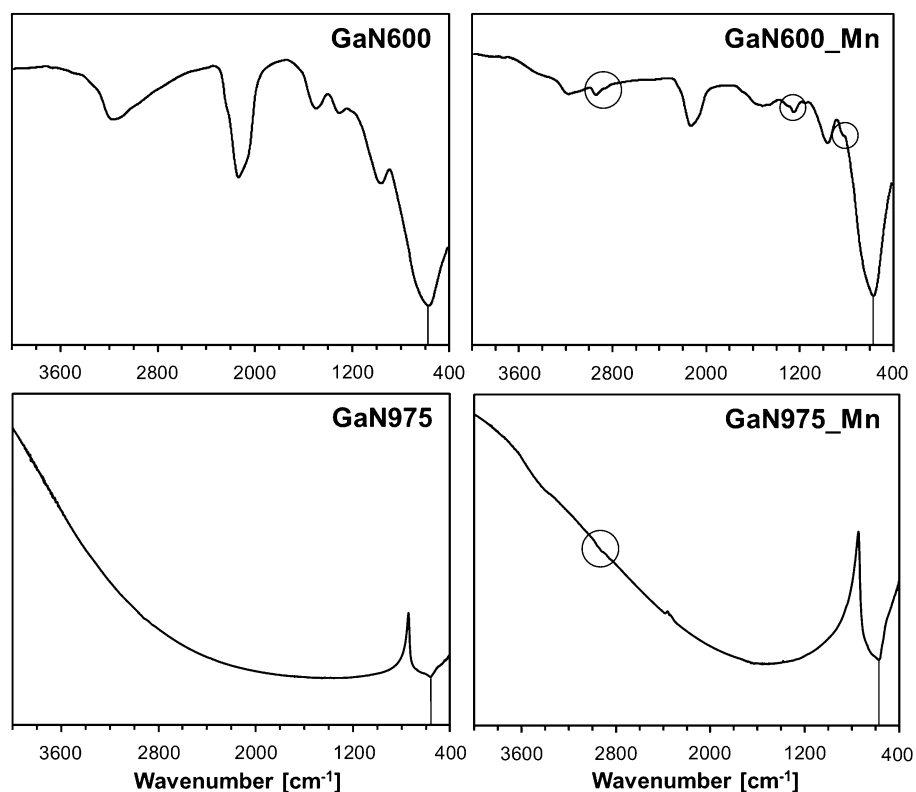

vibrations, likely, in adsorbed ammonia and –NH₂ surface groups. Both peaks decrease in their relative intensities for the Mn-functionalized sample supporting reactions with consumption of such groups. Of special interest is a group of weak peaks at 2850–2970 cm^{-1} and the bands at 1250 and 830 cm^{-1}, which are characteristic for vibrations in the residual trimethylsilyl groups, and which are clearly present in the spectrum for the Mn-functionalized 600 °C-derived material (Fig. 4, encircled areas). These bands are virtually absent (below the method detection limits) in the 975 °C-derived material supporting relatively higher quantities of adsorbed Mn precursor in the nanopowder with much higher surface area from the lower synthesis temperature (vide infra). Upon magnification, very weak bands in the region of 2850–2950 cm^{-1} can be seen just above noise level in the nanopowder from the highest synthesis temperature, too, which agrees with the above conclusion (Fig. 4, bottom right). The retention of some Mn-N[Si(CH₃)₃]₂ groups is consistent with incomplete transamination/deamination chemistry upon the applied treatment at 200 °C during Mn functionalization. These groups upon exposure to air may form Mn- and Si-containing oxidation by-products.

SEM examination provides a direct support for particle coating upon Mn functionalization as demonstrated in Fig. 5. This is especially well observed for the case of the 975 °C-derived materials (Fig. 5, bottom row)—the pure GaN975 powder shows numerous particles with well-evolved crystalline facets (for instance, see the area in the circles), whereas the resulting Mn-functionalized GaN975_Mn powder contains all rounded particles independent on their size. Since for the GaN600_Mn material, the observed particles are in fact crystallite agglomerates (a few nanometer in size crystallites are not discernible under standard SEM magnifications), the coating effect is not as clear. However, a detailed examination of the images supports a more compact structure upon Mn functionalization with a more regularly shaped particles, which is consistent with surface cladding.

The studies of helium density and BET specific surface area provide a very interesting insight into the porous nature of the materials (Table 2). Among the starting materials, the highest surface area S$_{BET}$ of 148 m^2/g is displayed by GaN600 from the lowest synthesis temperature, whereas the lowest one of 14 m^2/g is found for GaN975 from the highest synthesis temperature. Such a trend is commonly seen in

Figure 5 SEM morphology of GaN powders before (*left*) and after Mn surface functionalization (*right*). *Top row* 600 °C-derived materials, *bottom row* 975 °C-derived materials.
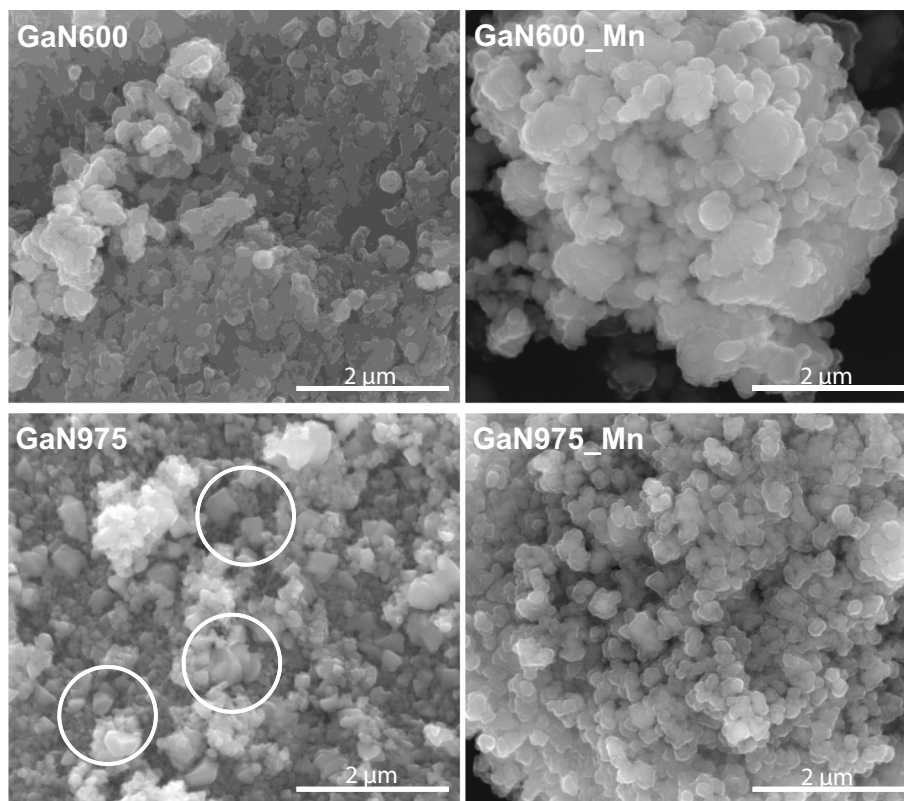
Table 2 Helium density d_{He} and BET specific surface area S_{BET} of GaN nanopowders before and after Mn surface functionalization

|	GaN600	GaN600_Mn	GaN800	GaN800_Mn	GaN900	GaN900_Mn	GaN975	GaN975_Mn
d_{He} (g/cm^3)	4.06	2.87	4.92	4.48	5.48	5.23	5.89	5.44
S_{BET} (m^2/g)	148	62	64	43	32	28	14	14
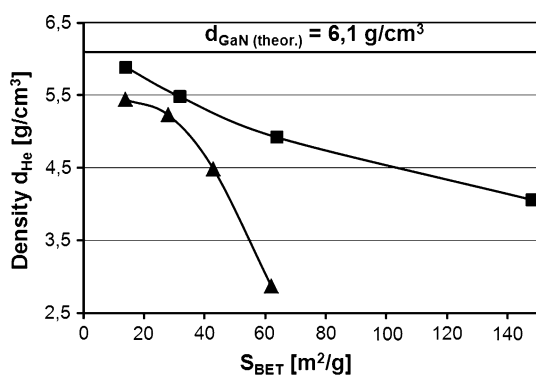
Figure 6 Helium density d_{He} *vs*. specific surface area S_{BET} for GaN nanopowders determined before (*squares*) and after (*triangles*) Mn surface functionalization. The *connecting lines* are guides for eye, only.

materials chemistry and is linked to increased crystallite sizes (and resulting decreased surface area)/recrystallization with temperature. The GaN600 is mesoporous, whereas GaN975 shows only remnant porosity typical for a collection of large crystallites with the remaining materials falling in between. The respective S_{BET} values generally get smaller upon Mn functionalization, e.g., from 148 to 62 m^2/g for GaN600_Mn or remain unchanged as in the case of GaN975_Mn. It is instructive to note that the surface area of crystalline materials such as nanocrystalline GaN originates mainly from the outer surface of crystallites or crystallite agglomerates since there is no place for a typical pore system such as encountered in highly amorphous carbons or in crystalline materials with a well-defined inner pore structure (zeolites, molecular sieves).

A characteristic trend is observed also for helium density changes. Namely, the helium density significantly falls with the decreasing average crystallite sizes/decreasing synthesis temperatures as already reported for a pool of similar GaN nanopowders [49].

Figure 7 XPS spectra in the Mn 2p energy range for selected Mn surface-functionalized GaN nanopowders; *left* GaN600_Mn, *right* GaN975_Mn. *Solid-line* curve peaking at ca. 646.5 eV is a shake-up satellite peak.
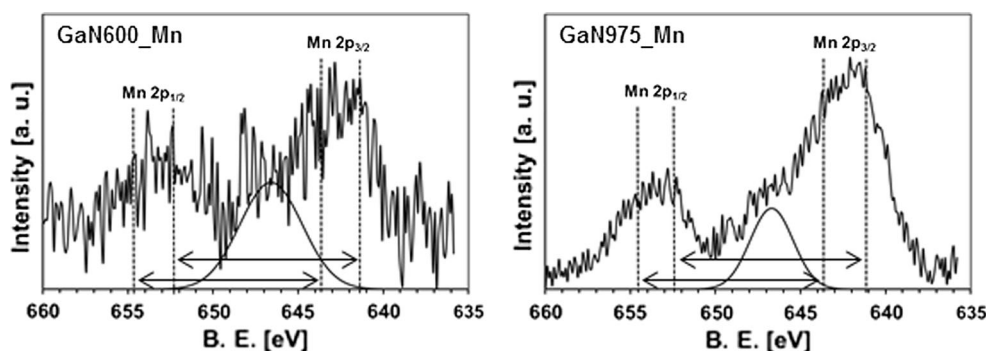
This phenomenon is associated with the presence of gas inaccessible pores in crystallite agglomerates. In this regard, the highest density in this study is 5.9 g/cm^3 to be compared with the theoretical value of 6.1 g/cm^3 for bulk GaN. The volume of the inaccessible pores appears to be a function of crystallite size and appropriately increases with the smaller sizes resulting in an apparent decrease of helium density. When looking into the effect of Mn functionalization, it is obvious that the densities become smaller compared to their respective values before. This is consistent with this step causing a noticeable blockage of some otherwise helium accessible spaces by a layer of the Mn-containing thin film formed on crystallite agglomerates/aggregates.

The changes of the S_{BET} and d_{He} for the starting and Mn-functionalized materials are shown in Fig. 6. For the starting nanopowders, there is approximately a linear relationship between these variables. There is clearly a pronounced influence of the Mn-modification step on both the helium density and BET specific surface area by blocking some otherwise gas accessible pores as discussed earlier. This causes a faster decrease of the helium density for the highest surface area materials. Actually, for the 900 and 975 °C-derived materials, i.e., for the largest average crystallite sizes among the nanopowders with remnant agglomeration, the curves/trends are closely paralleled and the BET surface areas of the starting and the related Mn-functionalized nanopowder do not differ much, if at all. A dramatic drop in both S_{BET} and d_{He} for the GaN600_Mn compared with the starting GaN600, i.e., the materials with the smallest average crystallite sizes, is consistent with a quite efficient blocking of pores of the then-prevailing agglomerates. This may result in much smaller quantities of the attached Mn in this nanopowder than anticipated based merely on its high BET specific surface area. In

other words, the high surface area probed by relatively small nitrogen molecules has little relevance to a surface area accessible by large molecules of the Mn precursor.

Direct evidence of a successful attachment of Mn species on GaN particles is provided by the surface-sensitive photoelectron spectroscopy XPS. All Mn-functionalized materials show up manganese, and two extreme examples of the Mn 2p$_{1/2}$ and 2p$_{3/2}$ spectral region are presented in Fig. 7. The noisy characteristics of both spectra are consistent with minute quantities of Mn in the samples as naturally expected here. In this regard, the relative Mn content in GaN600_Mn is clearly much lower than the Mn content in GaN975_Mn as judged by the signal-to-noise ratio. This is despite a much higher BET specific surface area of starting GaN600 compared to starting GaN975 (Table 2). However, as discussed above, the extensive agglomeration/aggregation of crystallites in GaN600 has apparently made part of the particle surface unavailable for interactions with the Mn precursor.

The rather broad and asymmetric peaks seen clearly for GaN975_Mn imply two different species. The deconvolution shows two pairs of component peak maxima as marked with the left right arrows. As far as the 2p$_{3/2}$ components at 641.1 and 643.8 eV are concerned, the first one is in the region of Mn^{2+} species, whereas the second one corresponds to manganese in higher oxidation states [50–53]. The Mn^{2+} ions with an unpaired electron in the d^5 configuration of high-spin paramagnetic state are further corroborated by the presence of a strong shoulder of a shake-up satellite peak at ca. 646.5 eV [51, 52]. The 2p$_{3/2}$ energies in the deconvoluted spectrum for GaN600_Mn are found at 641.2 and 643.8 eV; in this case, however, the very noisy spectrum prevents from similar conclusions about the satellite peak.

Figure 8 Optical spectra for selected starting and respective Mn surface-functionalized GaN nanopowders. *Top rectangular frame* 600 °C-derived samples, *bottom rectangular frame* 975 °C-derived samples. *Tangent lines* in the Kubelka–Munk transformed spectra (*right column*) are to visualize determinations of electronic transition energies.
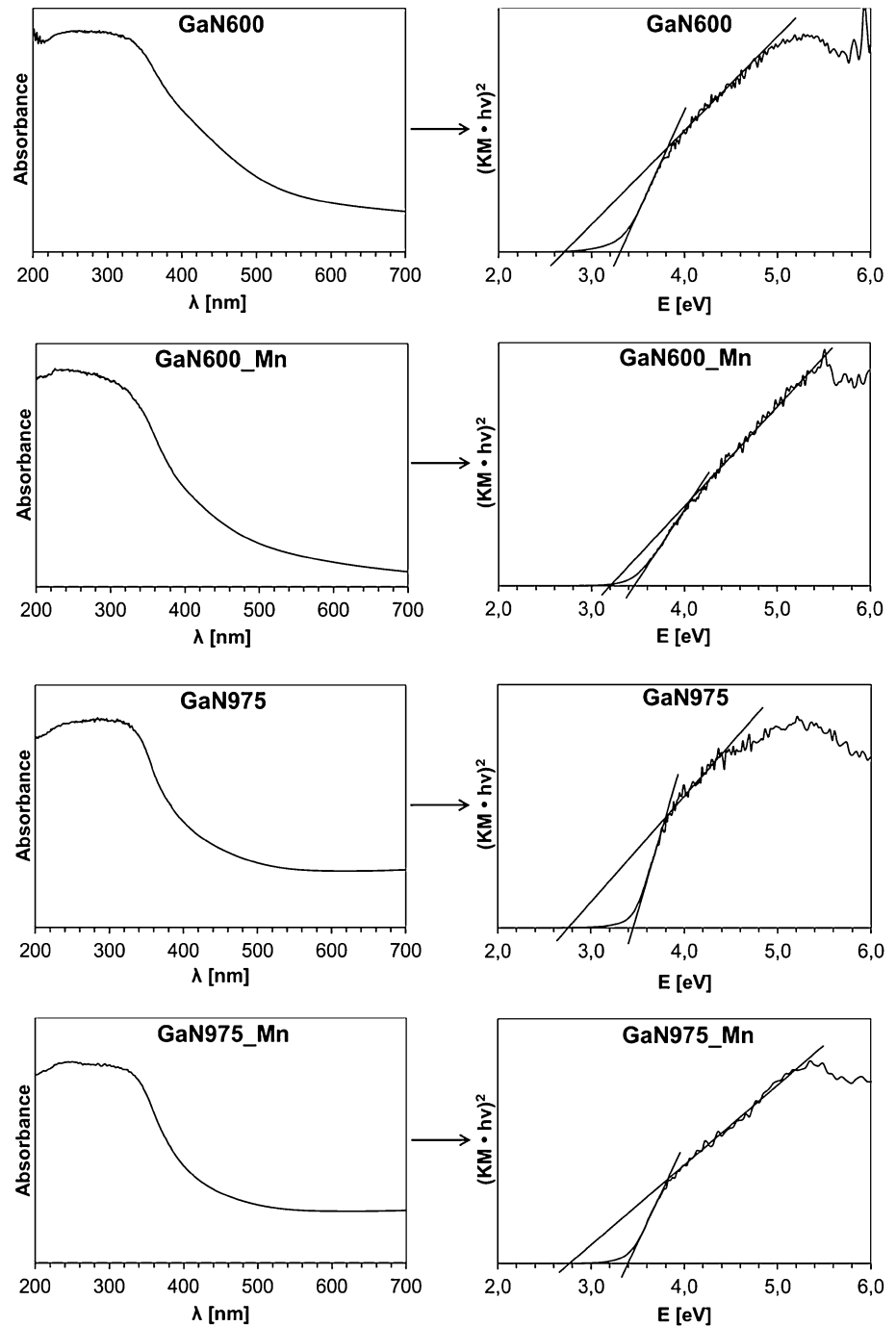
Alternatively, the broad Mn $2p_{3/2}$ peak in the original spectrum of each sample could be considered as belonging to only one Mn species with energy of ca. 642.5 eV, which is in the region of Mn^{3+}/Mn^{4+} oxidation states. In our opinion, the clear presence of the shake-up satellite peak mediates against such an option. In this regard, in one report, the Mn $2p_{3/2}$ peak energy at ca. 642 eV was assigned to manganese silicates $MnSiO_3/Mn_2SiO_4$ [53]. In conclusion, the XPS spectra are consistent with some of the Mn^{2+} ions being tetrahedrally incorporated within a thin gallium nitride surface layer. The excess of manganese precursor, which was initially nitrided during the synthesis step, appears to be converted to oxide-bearing derivative(s) in higher oxidation states. We want to note again that model chemistry in the

system manganese bis{bis[trimethylsilyl]amide}/ammonia affords manganese nitride η-Mn_2N_3 already at 150 °C, which shows to be prone to facile oxidation upon exposure to air [36].

The representative UV–vis spectra for the selected samples are shown in Fig. 8. The left column contains the original optical spectra (absorbance *vs.* wavelength) and the right one includes the respective Kubelka–Munk transformations that were used to derive specific electronic transitions. The transition energies for all nanopowders before and after Mn functionalization are included in Table 3. For gallium nitride, similarly as for Mn-doped hexagonal ZnO films, E_{g1} at the relatively lower energies corresponds likely to band tail transitions linked to various impurities, disorder, and defects, whereas E_{g2} is related to the material's energy bandgap [54]. One would anticipate, therefore, that the E_{g1} transitions could be somewhat sensitive to Mn functionalization by virtue of the resulting particle surface alteration.

Table 3 UV-vis-derived values of electronic transition energies for starting and Mn surface-functionalized GaN nanopowders

Samples	E_{g1} (eV)	E_{g2} (eV)
GaN600	2.66	3.31
GaN600_Mn	3.19	3.43
GaN800	2.40	3.20
GaN800_Mn	2.50	3.15
GaN900	2.45	3.31
GaN900_Mn	2.65	3.17
GaN975	2.67	3.42
GaN975_Mn	2.75	3.39

We also note that for bulk gallium nitride, the E_{g2} bandgap transitions are reported for h-GaN at ca. 3.4–3.5 eV and for c-GaN at 3.2–3.3 eV, whereas a shift to higher energies (blue shift) is expected for nanocrystallites with sizes below the Bohr radius quoted to be in the range 3–11 nm [55, 56].

From Table 3, it is apparent that there is some increase in the E_{g1} values when comparing the respective starting and the Mn-functionalized nanopowders. This increase is notably high for the 600 °C-derived materials, i.e., 0.53 eV, whereas for the remaining materials, it is in the range of 0.08–0.20 eV. What distinguishes the surface of GaN600 from the remaining nanopowders is the abundance of adsorbed gases but, mainly, of reactive functional groups such as Ga-NH_2 and Ga-NH-Ga (vide supra, TGA characterization) serving as efficient "anchors" for Mn precursor. We tentatively propose that the resulting surface layer made of Ga–N–Mn moieties introduces specific disorder/defects in the adjacent GaN lattice, which is then responsible for the observed E_{g1} shifts. The UV–vis study provides thus additional evidence for essential surface modifications via the systematically altered optical properties, which may be helpful in quantitative evaluation of the relevant electronic states. It is interesting to note that for some thick films of ZnO:Mn (hexagonal ZnO doped with 4 and 5 at.% Mn), similar E_{g1} shifts of the order of 0.2 eV were recorded [54].

The relatively high E_{g2} values linked to bandgap transitions for both 600 °C-derived materials reflect their phase inhomogeneous, mostly, cubic structures
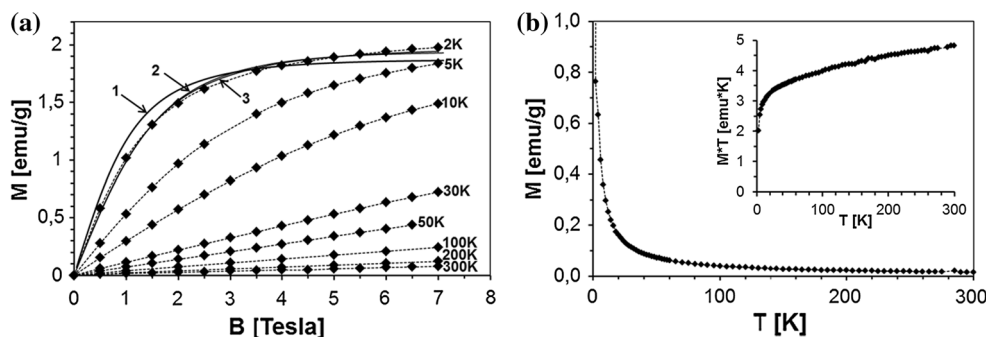
Figure 9 Magnetic measurements for sample GaN600_Mn. **a** Magnetization M as a function of magnetic field B at different temperatures. *Solid curve 1* Brillouin function at 2 K for S = 5/2, Mn content = 0.56 at.%; *solid curve 2* Brillouin function at 2 K for S = 1.56, Mn content = 0.93 at.%; *solid curve 3* Brillouin function at T_0 = 2.73 K for S = 5/2, Mn content = 0.59 at.%. **b** Magnetization M as function of temperature at magnetic field B = 1 Tesla; *inset* shows $M \cdot T$ *vs. T. Dashed lines* are guides for eye, only.
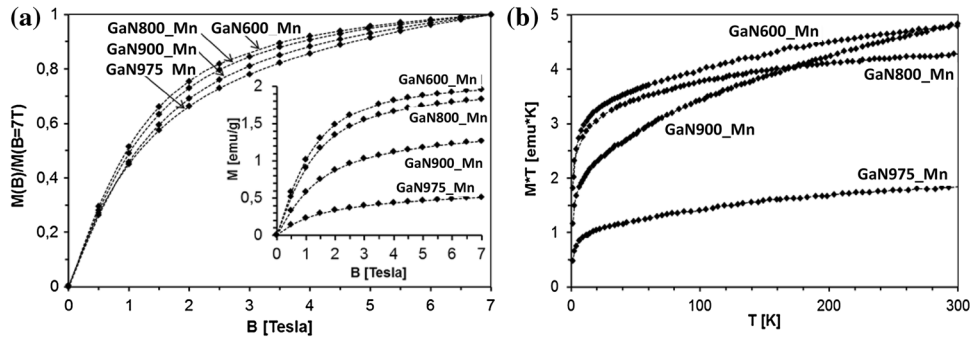
Figure 10 Magnetization data for all samples. **a** Normalized curves $M(B)/M(B = 7$ Tesla$)$ *vs.* magnetic field B at $T = 2$ K; *inset* shows magnetization as function of magnetic field at $T = 2$ K. **b** Magnetization measured as function of temperature and represented in the $M \cdot T$ *vs.* T coordinate system. *Dashed lines are guides for eye, only.*

[48] with the extremely small average crystallite sizes of 2 nm (Table 1). These values in the 3.31–3.43 eV range appear to be higher than expected for c-GaN (3.2–3.3 eV) and they are consistent with the blue shift phenomenon in this case, as discussed above. The range limits of E_{g2}, 3.15–3.31 eV, determined for the 800 and 900 °C-derived materials reflect the fact that these nanopowders are mixtures of c-GaN and h-GaN (Table 1). The predominantly hexagonal 975 °C-derived materials show the E_{g2} of 3.39–3.41 eV as expected for h-GaN. Except for the 600 °C-derived materials, there is a small decrease of the E_{g2} transition energies upon Mn functionalization but, we think, it is within the precision of energy determinations.

Magnetic properties of the Mn-functionalized nanopowders were of special interest as yet another way of looking into the nature of manganese species in the system. In this regard, a Mn ion substituting a Ga-site in GaN can exist in different charge states, depending on mutual position of the $Mn^{2+/3+}(d^5/d^4)$ level and the Fermi level. The ionized acceptor $Mn^{2+}(d^5)$ with five d-shell electrons is the most commonly observed configuration in GaN [57–59]. The spin of $Mn^{2+}(d^5)$-ions equals to $S = 5/2$ and the orbital momentum is $L = 0$. An isotropic paramagnetic behavior, which is typical for spin-only magnetic moment expected for $Mn^{2+}(d^5)$, was observed in n-type (Ga,Mn)N samples, both bulk [59, 60] and micropowders [61, 62]. On the other hand, the neutral acceptor configuration $Mn^{3+}(d^4)$ with four d-shell electrons was also observed in some GaN [59, 63, 64]. In this case, the magnetic moment originates mainly from spin $S = 2$ with some contribution of orbital momentum ($L = 2$). It was shown that highly resistive (Ga,Mn)N:Mg reveals a strong magnetic

anisotropy typical for the $Mn^{3+}(d^4)$ configuration [60]. This anisotropic behavior was successfully described by the crystal-field model. Naturally, mixtures of the $Mn^{2+}(d^5)$ and $Mn^{3+}(d^4)$ states in various proportions can be expected in (Ga,Mn)N depending on the position of the Fermi level [59, 60, 64].

For low Mn concentrations (below ca. 1 at.% Mn), the spins of magnetic ions are well separated from each other and any interaction among them is practically negligible. Consequently, magnetization of the $Mn^{2+}(d^5)$ ion system can be described by a standard Brillouin function with spin $S = 5/2$. On the other hand, an antiferromagnetic (AFM) d–d coupling was observed in n-type (Ga,Mn)N with higher Mn concentrations (above ca. 1 at.% Mn) [32, 61, 62]. Clear signatures of the AFM interaction are, first, a relatively slow saturation of magnetization with magnetic field (slower than expected for a standard Brillouin function) and, second, a Curie–Weiss-type behavior of susceptibility/magnetization in function of temperature. For instance, for (Ga,Mn)N with 9 at.% Mn, the determined Curie–Weiss temperature Θ was −12.5 K.

In general, all measured samples show an overall paramagnetic (PM) behavior. It should be stressed that there are no indications of the presence of ferromagnetic (FM) precipitates/clusters, commonly occurring in (Ga,Mn)N grown by other techniques [65]. Based on the current XRD data and similarities to the magnetic behavior of nanopowders/micropowders observed in our previous studies [32, 61, 62, 65], we ascribe the PM phase to the Mn ions incorporated on the surface of GaN nanograins. However, other residual magnetic phase/phases cannot be excluded. In particular, some AFM contribution to the total magnetization appears plausible.
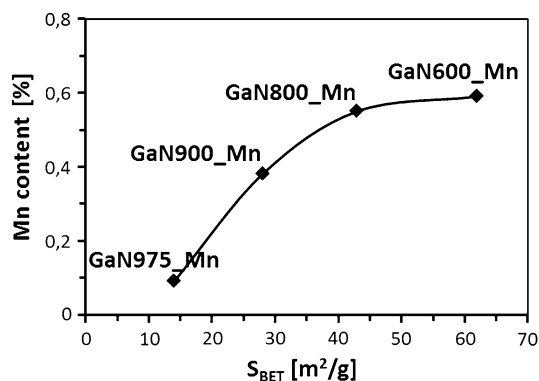
Figure 11 Mn content in the paramagnetic surface (Ga,Mn)N phase as function of S_{BET} of starting GaN nanopowders after Mn surface functionalization. *Connecting line* is a guide for eye, only.

The likely candidate for the AFM phase is manganese orthosilicate Mn_2SiO_4—an oxidation by-product of Mn excess-related residues from the synthesis [33–35, 66].

The representative magnetization results are shown in Fig. 9 for GaN600_Mn. A typical paramagnetic, Brillouin-like behavior is observed, i.e., magnetization tends to saturate with increasing magnetic field at the lowest temperatures, whereas at higher temperatures ($T > 50$ K), it is nearly linear with magnetic field. However, it is apparent that magnetization saturates with magnetic field much slower than predicted by a Brillouin function for $S = 5/2$ and non-interacting Mn ions (Fig. 9a, solid curve 1). A still better fit may be obtained if one allows the spin to be an adjustable parameter. In such a case, a reasonable fit is found for a spin close to 3/2 and a slightly higher Mn concentration (Fig. 9a, solid curve 2). We also note that equally good approximation is provided by a Brillouin function with $S = 5/2$ and effective temperature $T_{eff} = 2.73$ K, the latter higher by 0.73 K than the experimental temperature $T = 2$ K (Fig. 10a, solid curve 3 that virtually overlaps curve 2) [67]. In general, the observed deviations of magnetization from Brillouin function may result from several contributions.

First, they could be due to antiferromagnetic Mn–Mn exchange interactions. Second, they could stem from the presence of Mn ions in configurations different from $Mn^{2+}(d^5)$. We note that the p-type Mg-codoped (Ga,Mn)N single crystals of wurtzite structure have revealed strong magnetic anisotropy typical for $Mn^{3+}(d^4)$ ions [60]. In such a case, magnetization at $T = 2$ K and $B \perp c$, where c is

hexagonal axis, saturates with magnetic field nearly the same way as the Brillouin function with $S = 5/2$ does, whereas for B||c magnetization hardly saturates being almost linear in the range 2 Tesla $< B < 7$ Tesla. Thus, it can be anticipated that for randomly oriented nanoparticles, such as those in this study, magnetization originating from supposed $Mn^{3+}(d^4)$ centers should amount to the average of different orientations. This would result in slower saturation than for Mn ions in the $Mn^{2+}(d^5)$ configuration. And third, the observed deviations of magnetization could include a linear contribution originating from an AFM residual by-product such as mentioned earlier Mn_2SiO_4.

The data for all the measured samples are collected in Fig. 10 where in the left panel the scaled magnetization $M(B)/M$ ($B = 7$ Tesla) and the total magnetization (inset) are shown.

The largest magnetization per sample unit mass was found for GaN600_Mn, whereas the smallest for GaN900_Mn. On the other hand, the scaled magnetization data show that the rate of saturation of magnetization changes systematically with synthesis temperature—it is the largest for GaN600_Mn and the smallest for GaN975_Mn (Fig. 10a). Such an effect may result from either Mn–Mn d–d AFM interactions in the (Ga,Mn)N surface phase or/and a contribution of an AFM by-product phase. We note that the scaled magnetization of non-interacting ion systems (for both Mn^{2+} and Mn^{3+} ions) should be sample independent.

Further information may be extracted from magnetization measured as a function of temperature and plotted as $M \cdot T$ vs. T (Fig. 10b). It should be noted that for a purely paramagnetic, non-interacting system of magnetic moments, the function $M \cdot T$ vs. T does not depend on T if B/T is small ($M \cdot T$ vs. T should be a straight horizontal line), e.g., $T > 10$ K for $B = 1$ Tesla. Such a constant value of $M \cdot T$ is then related to the number of magnetic centers in the PM phase. On the other hand, specific interactions in the magnetic Mn-ion system (in the PM phase, i.e., not in the ordered phase) result in $M \cdot T$ vs. T curve bending—downward bending (i.e., $M \cdot T$ decreases with decreasing T) in the case of AFM interactions and upward bending for FM interactions.

Having in mind that Mn–Mn d–d AFM interactions of (Ga,Mn)N are not very strong (exchange constant for the nearest neighbors $J_{NN}/k_B = -1.9$ K [62]), one can ascribe the low temperature bending (for

Figure 12 Major steps in the preparation of GaN nanoparticles surface functionalized with manganese.

GaN nanoparticles
in Mn-precursor solution

work-up/nitridation

Mn-surface functionalized
GaN nanoparticles
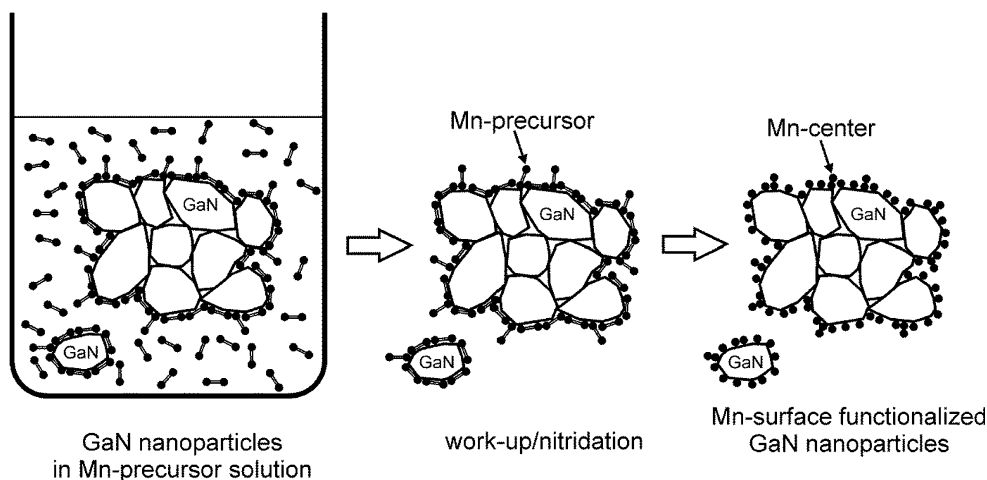
$T < 20$ K, Fig. 10b) to Mn–Mn interactions of Mn ions incorporated in the GaN surface layer, whereas the high temperature bending (for $T > 50$–100 K, Fig. 10b) to some by-product residues, most likely but not exclusively to the AFM phase of Mn_2SiO_4 mentioned above. The observed occurrence of the high temperature bending for all samples indicates the presence of the residual phase(s) in all of them. The largest residual phase contribution is observed for GaN900_Mn, whereas the lowest one for GaN800_Mn as approximated, among others, by slope of the experimental curves at high temperatures (Fig. 10b).

Due to the fact that the PM phase of (Ga,Mn)N and the AFM phase(s) of the residual by-product(s) show distinct magnetic behavior, the contribution of the PM phase can be extracted/estimated from the total measured magnetization. The details of the procedure are described elsewhere [33–35]. Herein, we assume that the measured magnetization is composed of a Brillouin function component (PM phase) and the magnetization of Mn_2SiO_4 (AFM phase). We note that the extracted PM contribution due to (Ga,Mn)N plotted as $M_{GaMnN} \cdot T$ *vs.* T appears to be a flat, horizontal line at high temperatures (not shown). The relevant constant value of $M \cdot T$ can subsequently be used for estimations of Mn ion concentration in the (Ga,Mn)N phase [33–35]. Neglecting the mass of the AFM by-product(s), which is a reasonable assumption here, and assuming $Mn^{2+}(d^5)$ configuration ($S = 5/2$), we arrive at the Mn contents of 0.59, 0.55, 0.38, and 0.09 at.% for GaN600_Mn, GaN800_Mn, GaN900_Mn, and GaN975_Mn, respectively. In this regard, if one assumes that the

Mn ions are in the $Mn^{3+}(d^4)$ configuration, the resulting Mn contents will be proportionally higher and, for instance, the content of 0.87 at.% is calculated for sample GaN600_Mn. However, to get a meaningful physical picture about the investigated nanopowders those values should be recalculated taking into account the fact that, actually, the Mn ions are incorporated in the surface layer of particles, of which thickness is at this point unknown. What is pretty much certain from the magnetic study, though, is that the Mn-containing paramagnetic phase resembles a relevant (Ga,Mn)N phase in our earlier studies on bulk Mn incorporation in GaN nanopowders. These similarities in magnetic behavior point out, now, to Mn ions rigidly anchored to the surface gallium nitride lattice in a way that allows for the overall paramagnetism and antiferromagnetic interactions among the ions. Therefore, the coupling of the magnetic and semiconducting properties, which is prerequisite for DMS materials, appears plausible for such modified nanopowders.

Figure 11 shows the Mn content of the PM phase in function of the BET specific surface area S_{BET} of starting nanopowders before Mn functionalization (Table 2). A saturation effect is observed for the S_{BET}'s higher than ca. 60 m^2/g, i.e., for nanopowders from the lower synthesis temperatures with the relatively high BET surface areas, GaN600_Mn and GaN800_Mn. This is consistent with definite diffusion barriers for spacious molecules of the Mn precursor, $Mn\{N[Si(CH_3)_3]_2\}_2$ (dimeric in the solid state), during Mn functionalization of the agglomerated/aggregated GaN nanocrystallites from precursor hexane solution—a significant part of the surface is

simply inaccessible to penetration by the precursor. A close to linear relationship between S_{BET} and Mn content for the nanopowders from the higher synthesis temperatures with the relatively low surface areas below ca. 40–60 m^2/g, from GaN975_Mn through GaN900_Mn up to GaN800_Mn, is a manifestation of a more open and accessible pore structure in these mostly mesoporous/macroporous materials made to a great extent of separate large nanocrystallites. It appears, therefore, that more complete particle Mn surface functionalization is achieved for the nanopowders with the relatively larger average particle sizes of the order of a few tens of nanometers and bigger, which do not form extensive crystallite agglomerates with inaccessible pores.

A mechanistic picture that emerges from the study is sketched in Fig. 12. It is consistent with a strong adsorption, likely, chemisorption of the Mn precursor on active sites of the GaN particle surface. The sites may include the Ga-NH$_2$ and/or Ga-NH-Ga amide/imide groups as well as a post-synthesis adsorbed ammonia as previously discussed. One can envision at least two Mn ion layers attached this way depending on the vertical or horizontal position of the dimer {Mn{N[Si(CH$_3$)$_3$]$_2$}$_2$}$_2$ "pointing" with its Mn centers toward the active sites of the GaN particle surface. This means that some excess of Mn remains in the system relative to a model Mn:N(surface) = 1 ratio. The 200 °C nitridation, which follows the precursor adsorption, removes most of the N[Si(CH$_3$)$_3$]$_2$ groups, especially, from the lower BET surface area nanopowders (relatively less agglomerated), whereas the lingering organic groups may partially decompose and be subjected to oxidation upon exposure to air. This can be a source of a residual Mn phase, such as Mn$_2$SiO$_4$, accompanying the surface built-in Mn ion-containing phase abbreviated earlier as (Ga,Mn)N.

Conclusions

The hexane solution of the manganese amide precursor Mn{N[Si(CH$_3$)$_3$]$_2$}$_2$ was effectively applied at ambient conditions to functionalize with manganese the surface of a range of GaN nanopowders. Following mild ammonolysis at 200 °C, the particle surface of individual crystallites and/or crystallite agglomerates was shown to contain the paramagnetic phase of the Ga-N-Mn type of lattice, which was

similar in magnetic behavior to the relevant bulk-modified (Ga,Mn)N nanopowders. The pool of GaN nanopowders with diverse surface properties afforded various Mn-functionalized nanopowders with a range of Mn contents, nominally, from approx. one tenth to a few tenth of at.% Mn. These Mn surface-functionalized GaN nanopowders upon process optimization may constitute a new class of diluted magnetic semiconductors. Some challenging questions in synthesis refinement still remain open including (1) the use of surface-adjusted concentrations of the Mn precursor to avoid by-product formation from precursor excess, (2) application of other Mn precursors, possibly, with more efficient transamination/deamination chemistry, and (3) maximizing an accessible particle surface by using dispersed particle systems of GaN quantum dots or breaking down the originally formed crystallite agglomerates with high-energy ball milling. A more refined approach to study adsorbed layer characteristics is also planned in the optimized follow-up investigations.

References

[1] Ariga K, Li J, Fei J, Ji QM, Hill JP (2016) Nanoarchitectonics for dynamic functional materials from atomic/molecular level manipulation to macroscopic action. Adv Mater 28:1251–1286

[2] Chen G, Roy I, Yang C, Prasad PN (2016) Nanochemistry and nanomedicine for nanoparticle-based diagnostics and therapy. Chem Rev 116:2826–2885

[3] Qi W (2016) Nanoscopic thermodynamics. Acc Chem Res. doi:10.1021/acs.accounts.6b00205

[4] Malgras V, Ji Q, Kamachi Y, Mori T, Shieh FK, Wu KCW, Ariga K, Yamauchi Y (2015) Templated synthesis for nanoarchitectured porous materials. Bull Chem Soc Jpn 88:1171–1200

[5] Zhao Z, Sun Y, Dong F (2015) Graphitic carbon nitride based nanocomposites: a review. Nanoscale 7:15–37

[6] Goswami S, Mondal AK, Konar S (2015) Nanoscopic molecular magnets. Inorg Chem Front 2:687–712

[7] Singh R (2013) Unexpected magnetism in nanomaterials. J Magn Magn Mater 346:58–73

[8] Arakawa Y (2002) Progress in GaN-based quantum dots for optoelectronics applications. IEEE J Sel Top Quant Elect 8:823–832

[9] Muramoto Y, Kimura M, Nouda S (2014) Development and future of ultraviolet light-emitting diodes: UV-LED will replace the UV lamp. Semicond Sci Technol 29:84004–84011

[10] Akasaki I, Amano H (1997) Crystal growth and conductivity control of Group III nitride semiconductors and their application to short wavelength light emitters. Jpn J Appl Phys 36:5393–5408

[11] Fareed RSQ, Hu X, Tarakji A, Deng J, Gaska R, Shur M, Khan MA (2005) High-power AlGaN/InGaN/AlGaN/GaN recessed gate heterostructure field-effect transistors. Appl Phys Lett 86(14):3512

[12] Navarro A, Rivera C, Pereiro J, Munoz E, Imer B, DenBaars SP, Speck JS (2009) High responsivity A-plane GaN-based metal-semiconductor-metal photodetectors for polarization-sensitive applications. Appl Phys Lett 94:213512–213514

[13] Ueda T, Ishida M, Tanaka T, Ueda D (2014) GaN transistors on Si for switching and high-frequency applications. Jpn J Appl Phys 53:100214

[14] Morkoc H (2009) Handbook of nitride semiconductors and devices. Wiley, Weinheim

[15] Felser C, Fecher GH, Balke B (2007) Spintronics: a challenge for materials science and solid-state chemistry. Angew Chem Int Ed 46:668–699

[16] Dietl T, Ohno H (2014) Dilute ferromagnetic semiconductors: physics and spintronic structures. Rev Mod Phys 86:187–251

[17] Awschalom DD, Flatté ME (2007) Challenges for semiconductor spintronics. Nat Phys 3:153–159

[18] Dietl T (2010) A ten-year perspective on dilute magnetic semiconductors and oxides. Nat Mater 9:965–974

[19] Bonanni A (2007) Ferromagnetic nitride-based semiconductors doped with transition metals and rare earths. Semicond Sci Technol 22:R41–R56

[20] Li JM, Zeng XL, Wei DP, Hu YB, Xu ZA (2014) A Cu^{2+} ion–F center complex view on the photoluminescence quenching and correlating ferrimagnetism in $(Cu_2^+/Cu_1^{2+})_{0.044}Zn_{0.956}O$ electrospun nanobelts. ACS Appl Mater Interfaces 6:4490–4497

[21] Dietl T, Ohno H, Matsukura F, Cibert J, Ferrand D (2000) Zener model description of ferromagnetism in zinc-blende magnetic semiconductors. Science 287:1019–1022

[22] Sato K, Dederichs PH, Katayama-Yoshida H (2003) Curie temperatures of III–V diluted magnetic semiconductors calculated from first principles. Europhys Lett 61:403–408

[23] Katayama-Yoshida H, Sato K, Fukushima T, Toyoda M, Kizaki H, Dinh VA, Dederichs PH (2007) Theory of ferromagnetic semiconductors. Phys Stat Sol (A) 204:15–32

[24] Sarigiannidou E, Wilhelm F, Monroy E, Galera RM, Bellet-Amalric E, Rogalev A, Goulon J, Cibert J, Mariette H (2006) Intrinsic ferromagnetism in wurtzite (Ga, Mn)N semiconductor. Phys Rev B 74:041306

[25] Bonanni A, Kiecana M, Simbrunner C, Li T, Sawicki M, Wegscheider M, Quast M, Przybylińska H, Navarro-Quezada A, Jakieła R, Wolos A, Jantsch W, Dietl T (2007) Paramagnetic GaN: Fe and ferromagnetic (Ga, Fe)N: the relationship between structural, electronic, and magnetic properties. Phys Rev B 75:125210

[26] Pearton SJ, Abernathy CR, Thaler GT, Frazier RM, Norton DP, Ren F, Park YD, Zavada JM, Buyanova IA, Chen WM, Hebard AF (2004) Wide bandgap GaN-based semiconductors for spintronics. J Phys Condens Matter 16:R209–R245

[27] Khludkov SS, Prudaev IA, Tolbanov OP (2013) Gallium nitride as a material for spintronics. Russ Phys J 55:903–909

[28] Szyszko T, Kamler G, Strojek B, Weisbrod G, Podsiadło S, Adamowicz L, Gębicki W, Szczytko J, Twardowski A, Sikorski K (2001) Growth of bulk $Ga_{1-x}Mn_xN$ single crystals. J Cryst Growth 233:631–638

[29] Li H, Song B, Bao HQ, Wang G, Wang WJ, Chen XL (2009) Ferromagnetism of Mn-doped GaN polycrystalline powders. J Magn Magn Mater 321:222–225

[30] Wei YY, Guo JM, Hou DL, Qiao S (2008) Preparation and properties of Mn-doped GaN powders. Solid State Commun 148:234–236

[31] Janik JF, Drygaś M, Czosnek C, Kamińska M, Palczewska M, Paine RT (2004) Carbothermally-assisted aerosol synthesis of semiconducting materials in the system GaN/Mn. J Phys Chem Solids 65:639–645

[32] Gosk JB, Drygaś M, Janik JF, Palczewska M, Paine RT, Twardowski A (2006) Magnetic and optical properties of (GaMn)N nanocrystalline powders prepared by the aerosol-lassisted vapour phase synthesis and anaerobic imide route methods. J Phys D Appl Phys 39:3717–3725

[33] Drygaś M, Janik JF, Bućko MM, Gosk J, Twardowski A (2015) Structural and magnetic properties of GaN/Mn nanopowders prepared by an anaerobic synthesis route. RSC Adv 5:37298–37313

[34] Drygas M, Janik JF, Musial M, Gosk J, Twardowski A (2016) Tuning the bimetallic amide-imide precursor system to make paramagnetic GaMnN nanopowders. Mater Chem Phys 180:172–183

[35] Drygaś M, Janik JF, Gosk J, Gierlotka S, Palosz B, Twardowski A (2016) Structural and magnetic properties of ceramics prepared by high-pressure high-temperature

sintering of manganese-doped gallium nitride nanopowders. J Eur Ceram Soc 36:1033–1044

[36] Drygas M, Bucko MM, Musial M, Janik JF (2016) Convenient synthesis of nanocrystalline powders of phase-pure manganese nitride n-Mn_3N_2. J Mater Sci 51:8177–8186. doi:10.1007/s10853-016-0094-2

[37] Czepirski L, Janik JF, Komorowska-Czepirska E, Wells RL (2002) Adsorption characteristics of powders of nanometric gallium nitride and aluminum nitride. Adsorpt Sci Technol 20:723–728

[38] Chaplais G, Kaskel S (2004) Porosity control in pre-ceramic molecular precursor-derived GaN based materials. J Mater Chem 14:1017–1025

[39] West C, Mokaya R (2009) Nanocasting of high surface area mesoporous Ga_2O_3 and GaN semiconductor materials. Chem Mater 21:4080–4086

[40] Drygaś M, Janik JF, Czepirski L (2013) Adsorption properties of nanocrystalline/nanoporous gallium nitride powders. Curr Nanosci 9:318–323

[41] Niewa R (2002) Nitridocompounds of manganese: manganese nitrides and nitridomanganates. Z Kristallogr 217:8R–23R

[42] Gokcen NA (1990) The Mn–N (manganese-nitrogen) system. Bull Alloy Phase Diagrams 11:33–42

[43] Suzuki K, Kaneko T, Yoshida H, Obi Y, Fujimori H, Morita H (2000) Crystal structure and magnetic properties of the compound MnN. J Alloy Compd 306:66–71

[44] Leineweber A, Niewa R, Jacobs H, Kockelmann W (2000) The manganese nitrides η-Mn_3N_2 and θ-Mn_6N_5 + x: nuclear and magnetic structures. J Mater Chem 10:2827–2834

[45] Feng WJ, Sun NK, Du J, Zhang Q, Liu XG, Deng YF, Zhang ZD (2008) Structural evolution and magnetic properties of Mn–N compounds. Sol State Commun 148:199–202

[46] Janik JF, Wells RL (1996) Gallium imide, {Ga(NH)$_{3/2}$}n, a new polymeric precursor for gallium nitride powders. Chem Mater 8:2708–2711

[47] Bradley DC, Hursthouse MB, Malik KMA, Moseler R (1978) The crystal molecular structure of "bis(hexamethyl-disilylamido) manganese". Transit Metal Chem 3:253–254

[48] Hwang JW, Campbell JP, Kozubowski J, Hanson SA, Evans JF, Gladfelter WL (1995) Topochemical control in the solid-state conversion of cyclotrigallazane into nanocrystalline gallium nitride. Chem Mater 7:517–525

[49] Drygaś M, Janik JF (2012) Modeling porosity of high surface area nanopowders of the gallium nitride GaN semiconductor. Mater Chem Phys 133:932–940

[50] Matienzo LJ, Yin LI, Grim SO, Swartz WE Jr (1973) X-ray photoelectron spectroscopy of nickel compounds. Inorg Chem 12:2762–2769

[51] Ivanova TM, Shchukarev AV, Naumkin AV, Sidorov AA, Kiskin MA, Novotortsev VM, Eremenko IL (2008) X-ray photoelectron spectra of polynuclear manganese complexes. Rus J Inorg Chem 53:1929–1933

[52] Wang ZY, Huang BB, Yu L, Dai Y, Wang P, Qin XY, Zhang XY, Wei JY, Zhan J, Jing XG, Liu HX, Whangbo MH (2008) Enhanced ferromagnetism and tunable saturation magnetization of Mn/C-codoped GaN nanostructures synthesized by carbothermal nitridation. J Am Chem Soc 130:16366–16373

[53] Swaminathan S, Spiegel M (2007) Thermodynamic and kinetic aspects on the selective surface oxidation of binary, ternary and quarternary model alloys. Appl Surf Sci 253:4607–4619

[54] Akyuz I, Kose S, Atay F, Bilgin V (2006) The optical, structural and morphological properties of ultrasonically sprayed ZnO: Mn films. Semicond Sci Technol 21:1620–1626

[55] Ramvall P, Tanaka S, Nomura S, Riblet P, Aoyagi Y (1998) Observation of confinement-dependent exciton binding energy of GaN quantum dots. Appl Phys Lett 73:1104–1106

[56] Chen XL, Li JN, Cao YG, Lan YC, Li H, He M, Wang CY, Zhang Z, Qiao ZY (2000) Straight and smooth GaN nanowires. Adv Mater 12:1432–1434

[57] Baranov PG, Ilyin IV, Mokhov EN (1997) Identification of iron transition group trace impurities in GaN bulk crystals by electron paramagnetic resonance. Solid State Comm 101:611–615

[58] Graf T, Gjukic M, Hermann M, Brandt MS, Stutzmann M (2003) Spin resonance investigations of Mn^{2+} in wurtzite GaN and AlN films. Phys Rev B 67:165215

[59] Wolos A, Palczewska M, Zajac M, Gosk J, Kaminska M, Twardowski A, Bockowski M, Grzegory I, Porowski S (2004) Optical and magnetic properties of Mn in bulk GaN. Phys Rev B 69:115210

[60] Gosk J, Zajac M, Wolos A, Kaminska M, Twardowski A, Grzegory I, Bockowski M, Porowski S (2005) Magnetic anisotropy of bulk GaN: Mn single crystals codoped with Mg acceptors. Phys Rev B 71:094432

[61] Zajac M, Doradzinski R, Gosk J, Szczytko J, Lefeld-Sosnowska M, Kaminska M, Twardowski A, Palczewska M, Grzanka E, Gebicki W (2001) Magnetic and optical properties of GaMnN magnetic semiconductor. Appl Phys Lett 78:1276–1278

[62] Zajac M, Gosk J, Kaminska M, Twardowski A, Szyszko T, Podsiadlo S (2001) Paramagnetism and antiferromagnetic dd coupling in GaMnN magnetic semiconductor. Appl Phys Lett 79:2432–2434

[63] Graf T, Gjukic M, Brandt MS, Stutzmann M, Ambacher O (2002) The $Mn^{3+/2+}$ acceptor level in group III nitrides. Appl Phys Lett 81:5159–5161

[64] Wolos A, Wysmolek A, Kaminska M, Twardowski A, Bockowski M, Grzegory I, Porowski S, Potemski M (2004)

Neutral Mn acceptor in bulk GaN in high magnetic fields. Phys Rev B 70:245202

[65] Zając M, Gosk J, Grzanka E, Stelmakh S, Palczewska M, Wysmołek A, Korona K, Kamińska M, Twardowski A (2008) Ammonothermal synthesis of GaN doped with transition metal ions (Mn, Fe, Cr). J Alloy Compd 456:324–338

[66] Hagemann IS, Khalifah PG, Ramirez AP, Cava RJ (2000) Geometric magnetic frustration in olivines. Phys Rev B 62:R771–R774

[67] Gaj JA, Planela R, Fishman G (1979) Relation of magneto-optical properties of free-exciton to spin aligment of Mn^{2+} ions in CD1-XMNXTE. Solid State Commun 29:435–438

Erratum

CrossMark

Erratum to: Nanopowders of gallium nitride GaN surface functionalized with manganese

Michał Musiał[1], Jacek Gosk[2], Andrzej Twardowski[3], Jerzy F. Janik[1], and Mariusz Drygaś[1,*]

[1] *Faculty of Energy and Fuels, AGH University of Science and Technology, al. Mickiewicza 30, 30-059 Krakow, Poland*
[2] *Faculty of Physics, Warsaw University of Technology, ul. Koszykowa 75, 00-662 Warsaw, Poland*
[3] *Faculty of Physics, Institute of Experimental Physics, University of Warsaw, ul. Pasteura 2, 02-093 Warsaw, Poland*

Erratum to: J Mater Sci
DOI 10.1007/s10853-016-0317-6

The original article contains an incorrect version of Fig. 8 (the rectangular frames separating the 600°C-derived samples from the 975 °C-derived samples were missing). The correct Fig. 8 is displayed below.

Address correspondence to E-mail: madrygas@agh.edu.pl

Figure 8 Optical spectra for selected starting and respective Mn surface-functionalized GaN nanopowders. *Top rectangular frame* 600 °C-derived samples, *bottom rectangular frame* 975 °C-derived samples. *Tangent lines* in the Kubelka–Munk transformed spectra (*right column*) are to visualize determinations of electronic transition energies.